High rejection and frequency tunable optical filtering of RF signals using a rare earth ion-doped crystal

Lothaire Ulrich, Sacha Welinski, Anne Louchet Chauvet, Julien de Rosny, Daniel Dolfi, Cyril Vaneph, Perrine Berger, Loic Morvan

IEEE OSA The Optical Society | Journal of Lightwave Technology

High rejection and frequency tunable optical filtering of RF signals using a rare earth ion-doped crystal

Journal:	*Journal of Lightwave Technology*
Manuscript ID	JLT-29382-2021
Manuscript Type:	Original Paper
Date Submitted by the Author:	30-Nov-2021
Complete List of Authors:	Ulrich, Lothaire; Thales Research and Technology France, Physics Department; Université Paris Sciences et Lettres, CNRS, Institut Langevin Welinski, Sacha; Thales Research and Technology France, Physics Department Louchet Chauvet, Anne; Université Paris Sciences et Lettres, CNRS, Institut Langevin, De Rosny, Julien; Université Paris Sciences et Lettres, CNRS, Institut Langevin Dolfi, Daniel; Thales Research and Technology France, Physics Department Berger, Perrine; Thales Research and Technology France, Physics Department Morvan, Loic; Thales Research and Technology France, Physics Department
Key Words:	Spectral Hole Burning, Microwave photonics, Filtering, Rare-earth doped Crystals
Category:	Microwave photonics, radio-over-fiber and optical wireless systems

High rejection and frequency tunable optical filtering of RF signals using a rare earth ion-doped crystal

Lothaire Ulrich, Sacha Welinski, Anne Louchet-Chauvet, Julien de Rosny, Daniel Dolfi, Perrine Berger, Loïc Morvan

***Abstract*—While photonics is broadly considered as a leading solution for analog RF processing, photonic RF filters often show a limited out-of-band rejection. In this work we demonstrate a high rejection and high steepness photonic RF bandpass filter based on spectral hole burning in a rare earth ion-doped crystal. The filter is obtained by programming a frequency-selective absorption grating in the crystal. With an experimental and theoretical study we identify the optimal parameters for this filter. We achieve a remarkable rejection of 60 dB and a rejection of 45 dB at 50 MHz from the edge of the filter, 20 dB higher than most photonic RF filters and compliant with most demanding applications.**

***Index Terms*—Spectral Hole Burning, Microwave photonics, Filtering, Rare-Earth Ion-doped Crystals.**

INTRODUCTION

THE growing congestion of the radio-frequency (RF) spectrum requires higher performances for systems aiming at monitoring the electromagnetic environnement. An ideal implementation of a monitoring system would proceed with the digitization of the full RF bandwidth followed by signal detection and recognition steps implemented in digital domain. High dynamic range full digitization remains however technologically challenging when the bandwidth exceeds 10 GHz, and also generates high data throughput [1]. The relevant signals can be buried in spurious tones, and the real-time, low-latency detection and recognition will also require a huge processing power. Depending on the targeted application, a tradeoff has then to be found between frequency resolution, bandwidth, dynamic range and probability of intercept of the signals.

Dealing with the current limitations of analog-to-digital converters (ADCs) leads to different practical alternatives to address very large bandwidths with a high dynamic range. The most prevalent solution is the superheterodyne architecture in which the input signal is mixed with a tunable local oscillator, as in most commercially available electronic sprectrum analysers. The signal is analyzed within a moderate bandwidth in which a high dynamic range digitization is possible. This method generally provides high resolution, bandwidth and dynamic range but low probability of intercept of the signals due to the sweep time, which is prohibitive for the detection of transient signals. Another option is to demultiplex the bandwidth by parallel RF filtering and then downconvert before digitization by multiple ADCs. This method provides large bandwidth and high probability of intercept of the signals, but often at the cost of a low interband dynamic range due to the currently limited steepness of RF filters [2], [3]. Sub-sampling is also implemented, especially at high RF frequencies [4], but shows a limited dynamic range or frequency bandwidth and possible signal ambiguity because of aliasing. Equivalent photonic-assisted solutions offer promising improvement especially for higher frequency range [3], [5]–[8] but still suffer from a trade-off between large instantaneous bandwidth, high dynamic range and high probability of intercept without ambiguity, in particular because of filtering performances. Rare-Earth Ion-doped Crystals (REIC) have shown their ability to overcome some of these limitations. By exploiting the high coherence of their optical transitions at low temperature and implementing Spectral Hole Burning (SHB) techniques, wideband spectrum analyzers exhibiting dynamic ranges up to 60 dB have been demonstrated over more than 20 GHz of instantaneous bandwidth with 100% of probabilty of intercept [9], [10].

However, a spectral analysis alone may not be sufficient to perform full signal recognition and could require more advanced pre-processing functions such as frequency filters, true time delays and down-converting stages [7], [11]. RF filtering in the optical domain is a valuable choice which allows to tune filters very quickly over a wide frequency band, due to the small bandwidth of the RF signals compared to optical frequencies. Besides, optical fibers make very high quality delay lines, which also is essential in RF processing. Yet, so far, optical RF filters have proven unsufficient rejection and edge steepness, due to the limited number of accessible filter poles. Although some optical processes such as Brillouin scattering [12] can provide higher rejection, most photonic filters present a rejection of at most 40dB [13], [14] or a rejection smaller than 30dB at 50MHz from the edge [15]–[17], while some stringent applications such as electronic warfare may require a rejection beyond 50 dB and a rejection larger than 40 dB at 50 MHz from the edge.

Lothaire Ulrich is with Thales Research and Technology, Palaiseau 91767, France and Paris Sciences & Lettres, CNRS, Institut Langevin, 75005 Paris, France.

Sacha Welinski, Daniel Dolfi, Perrine Berger and Loïc Morvan are with Thales Research and Technology, Palaiseau 91767, France. *Corresponding autor: Perrine Berger* (e-mail: perrine.berger@thalesgroup.com)

Anne Louchet-Chauvet and Julien de Rosny are with Paris Sciences & Lettres, CNRS, Institut Langevin, 75005 Paris, France

In this paper we present a photonic RF filter showing very high performances compatible with the most demanding applications, simultaneously in terms of rejection, steepness, low ripple and versatility, and compatible with the fast and wide tunability granted by optical architectures. This filter exploits the outstanding spectral properties of REIC, with almost no additional cost, size, weight and power consumption if combined with a SHB wideband spectrum analyzer. We first present a description of the filter, then explore experimentally the effects of different parameters, and finally present a model predicting the filter behavior. This study allows to discuss the key parameters determining the filter characteristics.

I. Setup

In this section we present the principle of the filter and the experimental setup. The core of the setup consists in a thulium doped YAG crystal maintained at 3 K in a closed-cycle cryostat. The doping concentration of the Tm^{3+} ions is 0.5 % (atomic), resulting in an optical depth $\alpha L \simeq 2$ for the ${}^3H_6 - {}^3H_4$ transition centered at 793.37 nm (in vacuum). The crystal is "programmed" (more explanations below) to diffract a selected range of optical frequencies only, which results in a band-pass filter on the diffracted beam. Our RF filter takes advantage of this optical filtering, as depicted in Fig.1. The RF input signal is transposed via a $LiNbO_3$ electro-optic intensity modulator onto an optical carrier tuned to the edge of the Tm^{3+} absorption line. The signal is filtered in the optical domain, recombined with the original carrier used as a local oscillator (LO), and acquired using a high-speed GaAs photodiode with a 5 dB loss at 20 GHz.

The programming stage relies on the Spectral Hole Burning (SHB) properties of the crystal, in order to engrave spectro-spatial gratings. SHB consists in optically adressing a fraction of the inhomogeneously broadened absorption profile (Fig.2.A). The optically excited population is transitorily transferred in a shelving state. This population storage creates a reduction of the absorption at the corresponding frequencies, resulting in holes in the absorption profile at the pumping frequency. A spectro-spatial interference pattern of illumination in the crystal is created by repeatedly sweeping a programming laser over a frequency interval $\Delta\nu_P$, split into two arms which are mixed in the crystal with a fixed angle and a relative delay τ (Fig.2.B and Fig.2.C). The delay improves the shape of the filter by making its impulse response causal, as detailed in section III. This method is a generalization of the use of pairs of linear frequency chirped pulses to create a spectral grating [18]. As illustrated in Fig.2.B, only the signal beam spectral components within $\Delta\nu_P$ experience the spectro-spatial gratings and are thus diffracted into a different direction: in that way, the desired frequencies are spatially extracted from the signal beam. Due to its finite lifetime, ranging from 10ms to 10s depending on the magnetic field and temperature [19], the grating needs to be periodically refreshed to be

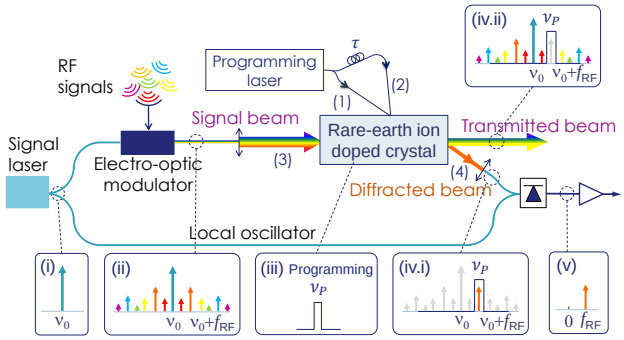

Fig. 1: Principle of the SHB filter – the signal laser (i) is modulated with the incoming RF signals, producing a symmetrical spectrum around the carrier's frequency (ii). The crystal is beforehand programed by the programming beams (1) and (2) to diffract the desired frequency band in a given direction (iii). After coupling towards free space the signal beam (3) goes through the crystal, resulting in a diffracted beam (4) containing the desired frequencies (iv.i) while the remaining frequencies are simply transmitted (iv.ii). After being coupled back into an optical fiber the diffracted beam is mixed with the LO – extracted from (i) – on a photodiode to demodulate the signal back to the RF range (v) and finally amplified by an electrical amplifier.

available at all times in the crystal. In our setup the crystal is cooled at 3 K in a closed-cycle cryostat in a 70 mT magnetic field. The programming time sequence is described in Fig.2.C.

II. Experimental results

A. Filter performances

We set up an SHB-based RF filter following the description in section I. We evaluate its performances with the help of a Vector Network Analyzer (VNA). Port 1 is connected to the filter input – the intensity modulator – and probes it with an RF signal at the desired frequency while Port 2 is connected to the filter output and acquires the system response at this specific frequency, providing the power transmission coefficient T. The curves are obtained by sweeping the stimulus frequency over the desired frequency band.

Fig.3 show the optimal SHB filter power transmission measured using our setup. With a global rejection of 60 dB and a rejection of 45 dB at 50 MHz from the edge, the rejection of the SHB filter is 20 dB better than most photonic filters found in the literature [13]–[17].

The choice of the experimental parameters leading to these performances is justified in the following by means of a parametric study (section II) and a theoretical model (section III). As we will see, the programming parameters dramatically influence the filter rejection and shape.

B. Rejection

The global rejection is the ratio between the transmission maximum within the filter band and the noise floor out of

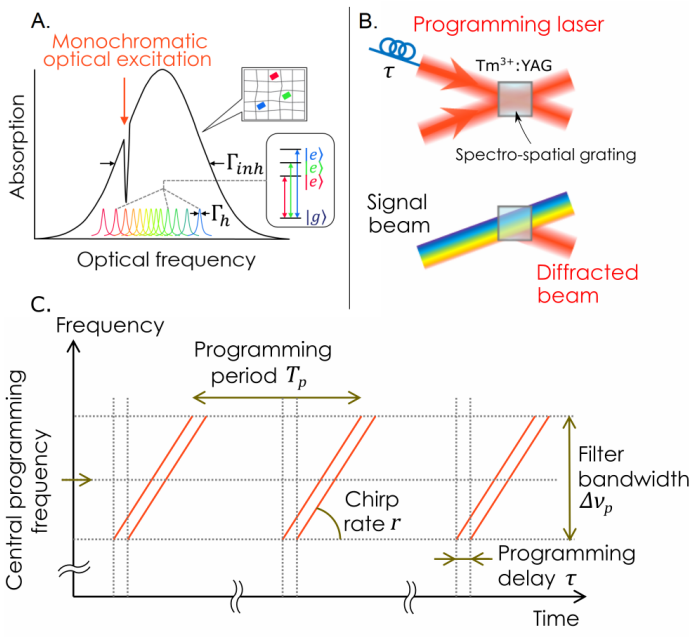

Fig. 2: A. Spectral hole burning in the inhomogenously broadened absorption line – Γ_h is the homogeneous width for the absorption line of a single Tm^{3+} ion, Γ_{inh} is the inhomogeneous width for the collective absorption of all Tm^{3+} ions, broadened by the crystal defects. In our 0.5 % doped crystal at 3K, $\Gamma_h \simeq 10$ kHz and $\Gamma_{inh} \simeq 20$ GHz;

B. programming the crystal – Spectro-spatial gratings over the frequency range $\Delta\nu_P$ are created by SHB using a programming laser splitted into two arms, interfering with a fixed angle, while its frequency is swept over $\Delta\nu_P$. The signal beam is sent through the crystal, only the signal beam spectral components within $\Delta\nu_P$ experience the spectro-spatial gratings and are thus diffracted into a different direction;

C. Time sequence of the programming beams reaching the crystal - The programming laser is chirped over the desired bandwidth and split into two arms, one of which undergoes the programming delay τ, then both arms are mixed on the crystal. This pattern is repeated periodically to maintain the grating in the crystal.

band. In the following we address successively these two features.

Considering that the RF input voltage is low compared to the modulator RF half-wave voltage V_π, the RF transmission can be written as derived in appendix A:

$$\frac{P_{\text{out}}}{P_{\text{in}}} \propto P_0^2 \left(\frac{\pi}{V_\pi}\right)^2 Z_{\text{MZM}} \eta_{\text{diff}} \mathcal{R}_L^2 G R \qquad \text{(II.1)}$$

where P_0 is the signal beam optical power, Z_{MZM} is the input impedance of the intensity modulator, η_{diff} is the diffraction efficiency of the crystal, $\mathcal{R}_L$ is the photodiode responsivity, G is the post-photodiode amplification and R is the resistive load of the receiver. In our setup P_0 = 10 mW, V_π = 1.4 V, $\mathcal{R}_L$ = 0.4 A/W and G = 36 dB.

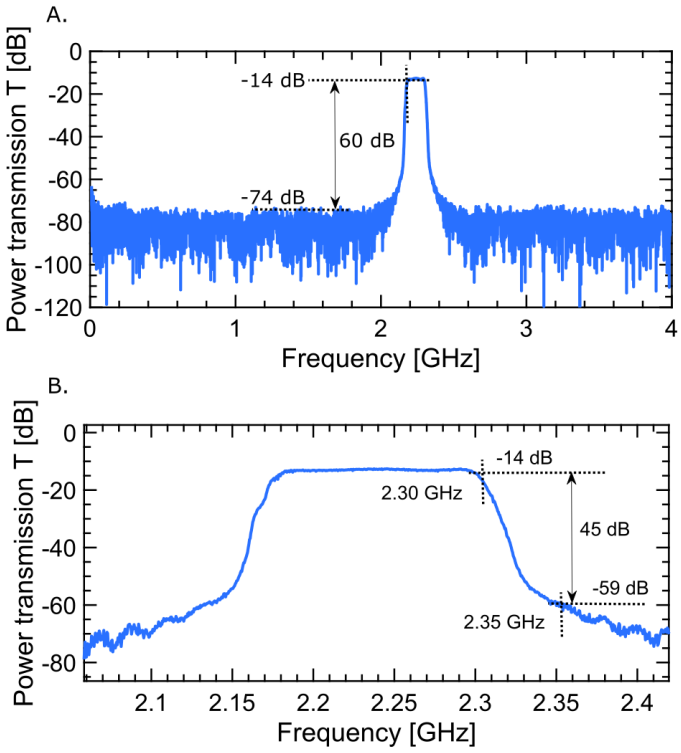

Fig. 3: A. SHB filter power transmission T with a set of optimal parameters as described in section II, providing a global rejection of 60dB, a rejection of 45 dB at 50 MHz from the edge; B. Close up on the filter of A.

Equation (II.1) emphasizes the importance of the diffraction efficiency in the SHB filter. We are in the "large angle" case defined in [19] in which a model of diffraction efficiency is developped. This model provides an upper bound to the diffraction efficiency with a theoretical diffraction efficiency of 11.6%, assuming a weak excitation and an optical depth set at an optimum value of 1.8. In such conditions a diffraction efficiency of 6.3 % was experimentally demonstrated [19]. Our experiment is similar to this previous demonstration except for the programming bandwidth which is much larger (between 100 MHz and 20 GHz). With a 100 MHz bandwidth we reached a diffraction efficiency of 2 %. This discrepancy originates from the imperfect grating contrast due to the temperature elevation within the crystal, caused by the strong excitation over a large bandwidth.

Fig.4 exhibits the noise floor level in different configurations. The green curve is obtained by switching off the diffracted beam and the LO (see Fig.2.D). It displays the noise brought by the RF reception chain (photodiode, amplifier and VNA). The detection of only the LO by the photodiode significantly increases the noise floor (red curve). Adding the diffracted beam (normal configuration of the SHB filter) does not increase further the noise floor (blue curve). This indicates that the noise floor of the filter is only brought by the LO. A compatible explanation is that the noise floor is produced by the GHz-range laser relative intensity noise (RIN) of the

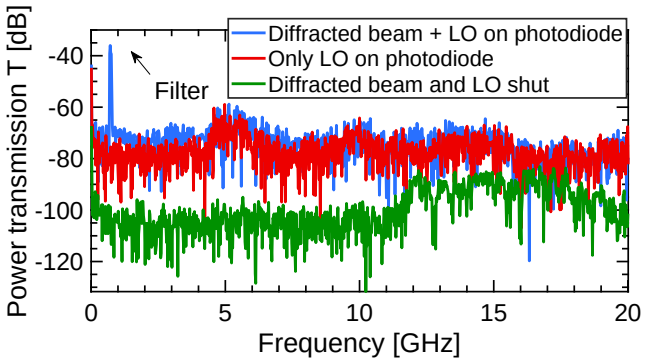

Fig. 4: Power transmission T when the diffracted beam and LO are shut (green), with only LO (red) and in normal configuration with LO and diffracted beam (blue), the filter being centered at 700 MHz. The curve was taken before filter optimization, which explains the low rejection.

local oscillator. In that case, as long as the RIN of the local oscillator is much higher than the next limiting noises (thermal, electronic, digital), reducing the RIN of the Signal Laser would proportionally reduce the noise floor, hence improve the rejection of the filter.

C. Filter shape

Beside the rejection, the filter shape is also critical. Ideally, it should be as square as possible, with steep sides to reject efficiently frequencies close to the edge, and a flat top to avoid distortions of the transmission through the filter.

The key parameter affecting the filter shape is the delay τ between the two programming beams (see Fig.2). Fig.5 shows that smaller delays can degrade the filter rejection up to 35 dB at a few hundreds of MHz from the edge, and alter the filter top shape. When increasing the delay from 0.1 ns to 48.2 ns, the sides of the filter become progressively steeper, and its top goes from a convex to a concave shape before finally reaching a flat shape. For larger delays ($>$ 48.2 ns) the overall filter shape remains rather constant (data not shown). This means that, beyond this delay, other mechanisms limit the steepness of the sides. We observe oscillations at the tails of the 11.5 ns and 48.2 ns delay curve whose period is $1/\tau$, reminiscent of the phase noise of a laser filtered by an interferometer. We conclude that the phenomenon limiting the sides steepness for long delays is the phase noise of the programming laser. In practice, we use in our setup a delay of 48 ns, i.e. 10 m of optical fiber, which provides the remarkable rejection of 45 dB at 50 MHz from the edge.

III. Theoretical model

To get more insight on the filter shape and to understand the influence of the different parameters mentioned above, we developed a theoretical semiclassical approach using the Optical Bloch Equations and the wave equation considering an optically thin crystal and a low programming optical power. The model, whose complete demonstration is presented in appendix B, yields the RF transfer function of the filter:

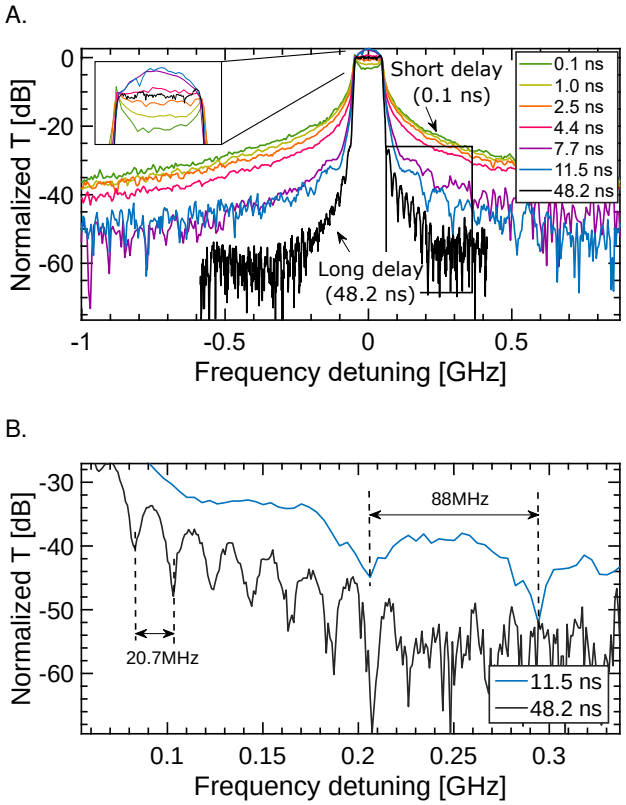

Fig. 5: A. Power transmission T of a 100 MHz wide filter for a wide range of programming delays τ. The delays are given $\pm$0.1 ns;

B. Close-up on the framed area for $\tau = 11.5$ ns and $\tau = 48.2$ ns. The period of the oscillations at the tail of the filter is close to $1/\tau$: 1/20.7 MHz = 48.3 ns and 1/88 MHz = 11.4 ns.

$$H\left(\nu + (\nu_P - \nu_0)\right) \propto \left[\left(|\tilde{A}_1|^2 e^{2i\pi\nu\tau}\right) \otimes \mathcal{L}_h \otimes \mathcal{L}_h \otimes \tilde{Y}\right](\nu) \quad \text{(III.1)}$$

where ν is the RF frequency, ν_P is the central optical frequency of the filter, ν_0 the signal laser frequency, $\tilde{f}$ the Fourier transform of f, $\mathcal{L}_h$ the lorentzian homogeneous lineshape of the optical transition ${}^3H_6 - {}^3H_4$ of Tm^{3+} and Y the Heaviside function. A_1 is the complex amplitude of the electric field of the first programming beam $E_1(t) = A_1(t)e^{i(\vec{k}_1\cdot\vec{r}-\omega t)}$. τ is the programming delay. We remind the reader that the second programming beam is a replica of the first pulse delayed by τ and propagating along the wavevector $\vec{k}_2$.

We see that the transmission is given by the engraving field convoluted twice by the homogeneous linewidth – once for the programming step, once for the read-out – and convoluted by the Heaviside causality function. Equation (III.1) is consistent with other results from the literature [20]. The power transmission of the filter is given by $T = |H|^2$.

In Fig.6 we compare experimental and simulated power transmissions for different delays. The model is in excellent agreement with the experimental curves, despite a weak

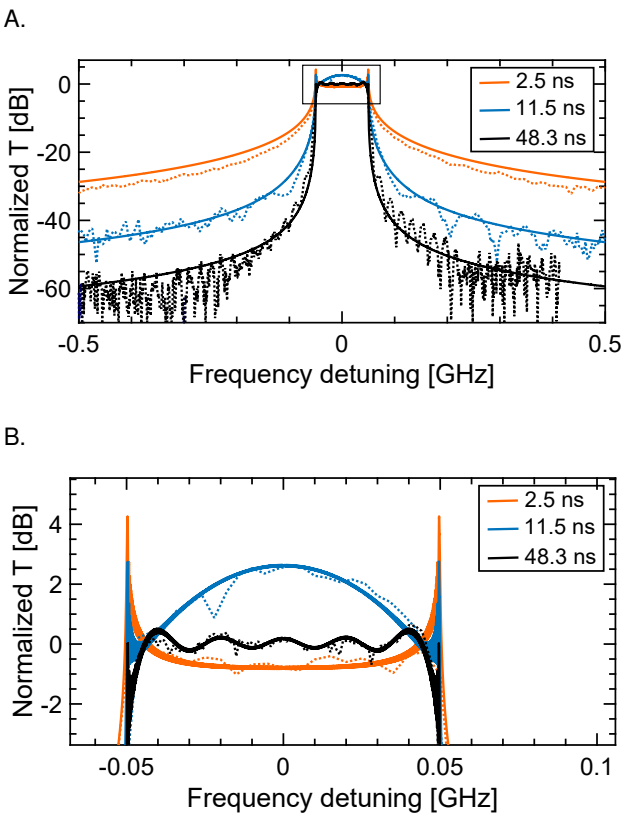

Fig. 6: A. Experimental (full line) and theoretical (dashed line) normalized power transmission T for three curves from Fig.5: 2.3 ns (orange), 11.4 ns (light blue), 48.3 ns (dark blue);
B. Close-up on the framed area from A.

discrepancy outside the bandpass range for lower delays (e.g. 2.5 ns curve from Fig.6.A). To perfectly match the experiment for small delays, the model should be fed with a delay approximately 1 ns larger than the one measured experimentally. Note that the oscillations on the wings are not reproduced, as we did not include any laser phase noise in the model. This could be taken into account by adding a random phase factor $e^{i\varphi(t)}$ in A_1 (see equation (III.1)).

In order to get more insight on the effect of the programming delay τ on the filter broadening, we rewrite equation (III.1). The 10 kHz homogeneous linewidth being much narrower than the programming bandwidth and the spectral period of the excitation $1/\tau$, the convolution by the lorentzian lineshapes can be neglected. We obtain:

$$H(\nu') \propto \left[\left(|\tilde{A}_1|^2 e^{2i\pi\nu\tau}\right) \otimes \tilde{Y}\right](\nu) \qquad \text{(III.2)}$$

where ν' corresponds to $\nu + (\nu_P - \nu_0)$. Using the Fourier transform operator F we can rewrite (III.2):

$$H(\nu') \propto F\left[F^{-1}\left[|\tilde{A}_1|^2 e^{2i\pi\nu\tau}\right](t) \times Y(t)\right](\nu) \qquad \text{(III.3)}$$

$$\propto F\left[F^{-1}\left[|\tilde{A}_1|^2\right](t-\tau) \times Y(t)\right](\nu) \qquad \text{(III.4)}$$

In (III.4) we have written the transfer function H as the Laplace transform of $F^{-1}\left[|\tilde{A}_1|^2\right](t-\tau)$. By definition, the impulse response is then given by $F^{-1}\left[|\tilde{A}_1|^2\right]$, translated towards positive times by τ. We can distinguish two cases:

- If τ is shorter than the duration of the impulse response $F^{-1}\left[|\tilde{A}_1|^2\right]$, the Heaviside function Y truncates it from $t = 0$. The causality only gives access to the part of the impulse response contained in positive times. This results in the spectral broadening observed in Fig.5.
- When τ exceeds the duration of $F^{-1}\left[|\tilde{A}_1|^2\right]$, its domain is fully contained in the positive times. We can then discard Y and we have with (III.3):

$$H(\nu') \propto |\tilde{A}_1|^2(\nu) \times e^{2i\pi\nu\tau} \qquad \text{(III.5)}$$

The transmission is the given by the power spectral density of the engraving field $|\tilde{A}_1|^2$, with a delay τ.

The typical time constant of the impulse response is the inverse of the filter bandwidth. In particular, it does not depend on the chirp rate. Note that, in the SHB filter, it is possible to choose a delay τ longer than the duration of the impulse response thanks to the long coherence time of the optical transition in the thulium ions, allowing to work in the photon echo regime [20].

In addition to the filter broadening, the programming delay τ also impacts the flatness of the filter's top. Using the theoretical model, we can compute for each delay the rejection and the geometric standard deviation of the transmission in the bandpass range. This is shown in Fig.7.A. and B. for a filter bandwidth of 1 GHz. We arbitrarily choose thresholds in terms of rejection and flatness defining our performance criteria (see caption of Fig.7). We can see that in such conditions both criteria are fulfilled for $\tau > 7$ ns. As we change the filter bandwidth, this minimal delay varies. Fig.7.C. depicts this variation: the minimal acceptable delay increases when the bandwidth is reduced. Indeed, as we see in (III.4), a reduced bandwidth increases the duration of the impulse response, which then requires a longer delay to translate to positive times. In order to work with a range of bandwidths, one should choose a delay providing a satisfactory shape for the smallest bandwidth.

IV. Discussion

The parametric study presented in this article resulted in remarkable rejections. Nevertheless we believe that this rejection can be further improved. As discussed in section II-B, the RIN of the signal laser limits the noise floor of the filter. This could be solved by using a laser with lower RIN, or by filtering out this noise, for example using SHB techniques [21]. This would improve the rejection of the filter

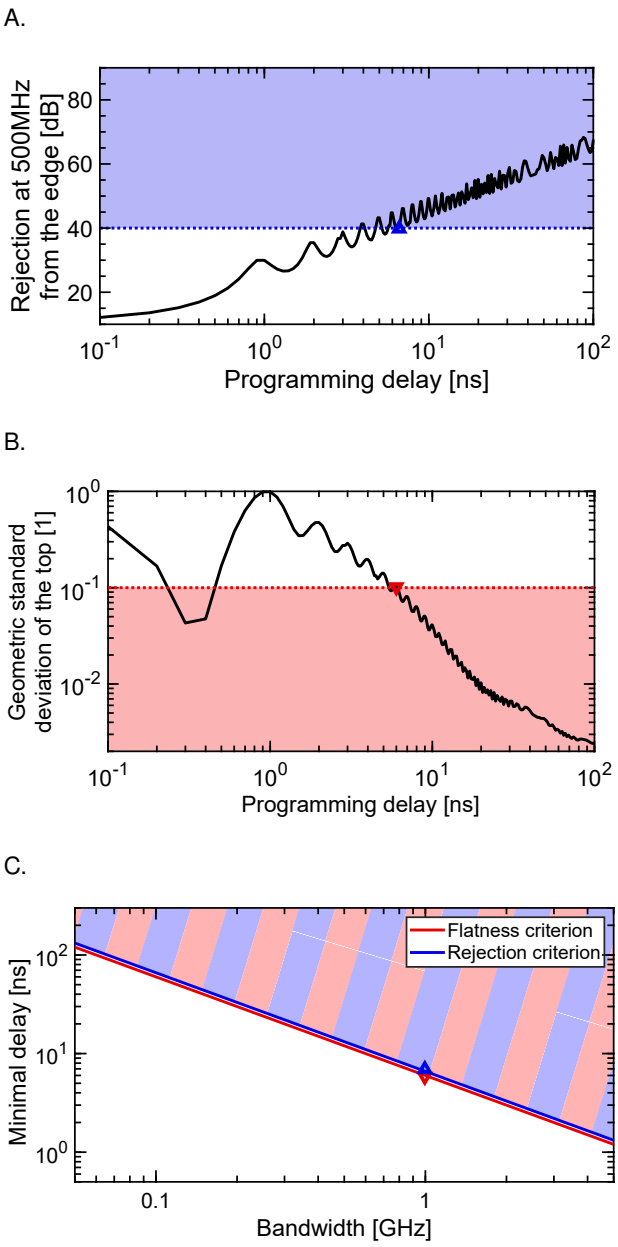

Fig. 7: A. Calculated rejection at 500 MHz from the edge of a 1 GHz-wide filter versus programming delay τ ; Blue area: area fulfilling the rejection criterion (rejection at 50% of the bandwidth $>$ 40 dB) ; Blue triangle: delay above which all delays fulfill the criterion;

B. Geometric standard deviation on 98% of the top of a 1 GHz filter, versus programming delay τ; Red area: area fulfilling the flatness criterion (deviation $<$ 0.1) ; Red triangle: delay above which all delays fulfill the criterion;

C. Evolution of the criteria with respect to filter bandwidth. The colored region corresponds to the range of delays where both criteria are satisfied : flatness – geometric standard deviation on 98% of the bandwidth below 0.1 – and rejection – rejection above 40 dB at 50% of the bandwidth from the edge.

of at least 10 dB . The rejection can also be enhanced by increasing the diffraction efficiency in the crystal. The latter can be improved by having a better control of the crystal temperature, especially when high optical power is used for programming.

It is possible to tune very quickly the central frequency of the SHB filter over a large bandwidth. As shown in Fig.1 insert (iv.ii), the RF filter's center frequency is given by the detuning $|\nu_P - \nu_0|$ between the programming laser and the signal beam carrier, which is largely tunable.

There are other assets also very specific to our SHB filter. First, many RF filters architectures, such as coupled cavities, exhibit a periodic frequency response, which can create ambiguities with higher frequencies signals. This is not the case with the SHB filter which is intrinsically non periodic. Second, the shape of the SHB filter is very versatile, since it is defined by the programming chirp as described in section I. This chirp can indeed be tailored into any desired shape within the 20 GHz inhomogeneous width of the crystal. For instance filtering multiple frequency bands with arbitrary bandwidths or making a notch filter is possible. However, since it requires the population stored into the shelving state to go back to thermal equilibrium, reconfiguring the shape of the filter is not as quick as tuning its center frequency, and depends on the shelving state's lifetime.

Finally, full characterisation of the filter requires both magnitude and phase response. The stabilization of the phase requires phase-locking the local oscillator with respect to the diffracted beam (see Fig.1). The study of the phase transmission will be the object of further work on the SHB filter.

V. Conclusion

We have demonstrated a photonic RF filter using a Rare-Earth ion Doped Crystal and its Spectral Hole Burning properties. This filter reaches outstanding performances compared to photonic RF filters, with a global rejection of 60 dB and a rejection of 45 dB at 50 MHz from the edge. Its shape can be customized over a 20 GHz band and very quickly tuned at any RF frequency. Those properties are remarkably well described by the theoretical model derived in this paper, which allowed us, along with the experimental study, to determine a set of relevant parameters to optimize the filter performances.

Although the experiment is quite heavy for a simple RF filter, our SHB filter can easily be combined with an SHB Wideband Spectrum Analyser in order to improve the processing functions, granting the Analyzer with a very high quality RF filter with almost no additional cost, size, weight and power consumption, and compatible with a down-converting stage or/and a stabilized delay line.

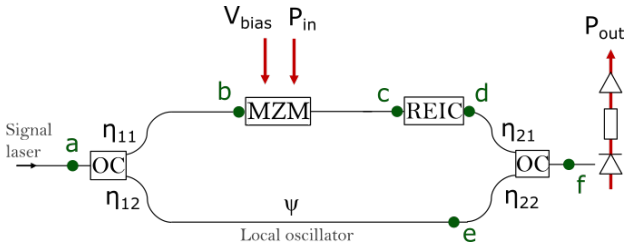

Fig. 8: Schematic description of the filter for power balance derivation of Appendix A. Black line: optical path, Red line: electrical path, MZM: Intensity modulator, REIC: Rare-Earth Ions doped Crystal, OC: Optical Coupler with field coupling ratio noted above and below. ψ is the phase difference between the local oscillator (lower path) and the active path (upper path). R is the internal load of the photodiode of responsivity η_{PD} and G the electrical amplification gain. The oscillating part of the input tension $V(t)$ applied to the phase modulator is equivalent to an RF input power P_{in} . In appendix A we derive $P_{\text{out}}/P_{\text{in}}$.

APPENDIX A
POWER TRANSMISSION OF THE SHB RF FILTER

We derive the power transmission of the SHB RF filter. Fig.8 depicts a schematic description of the filter. In the following, $E_k(t)$ will denote the electric field at point k. The signal laser is the optical input $E_a(t) = E_0 e^{i\omega t}$.

The voltage applied to the intensity modulator (MZM) has an RF part : $V_{RF}\sin(\omega_{RF}t)$, and a DC part : V_{bias}. We set V_{bias} such that even orders of modulation are suppressed by destructive intereference. After the MZM we get :

$$E_c(t) = -\frac{1}{2}\eta_{11}E_0 \sum_{n\in Z^*} J_n(\beta)e^{i(\omega+n\omega_{RF})t} \tag{A.1}$$

where J_n is the Bessel function of order n and $\beta = \pi V_{RF}/V_{\pi,RF}$ is the modulation index .

The purpose of the optical filter performed by the crystal is to select the first harmonic of the modulation by diffraction. The losses induced by this process are described by the diffraction efficiency η_{diff}:

$$E_d(t) = -\frac{1}{2}\eta_{11}\eta_{\text{diff}}E_0 J_1(\beta)e^{i(\omega+\omega_{RF})t} \tag{A.2}$$

With ψ the phase difference between the local oscillator and the active path we find:

$$\begin{aligned} E_f(t) &= \eta_{22}E_e(t) + \eta_{21}E_d(t) \\ &= \eta_{22}\eta_{12}e^{i\psi}E_0 e^{i\omega t} - \eta_{21}\frac{1}{2}\eta_{11}\eta_{\text{diff}}E_0 J_1(\beta)e^{i(\omega+\omega_{RF})t} \end{aligned} \tag{A.3}$$

The oscillating part of the current produced by the photodiode under the electric field E_f reads:

$$\begin{aligned} I_{RF}(t) &= \eta_{PD}\times 2\Re\left[\left(-\eta_{22}\frac{1}{2}\eta_{12}\eta_{\text{diff}}E_0 J_1(\beta)e^{i(\omega+\omega_{RF})t}\right)\right. \\ &\quad \left.\times\left(\eta_{21}\eta_{11}e^{i\psi}E_0 e^{i\omega t}\right)^*\right] \\ &= -\eta_{11}\eta_{12}\eta_{21}\eta_{22}\ \eta_{PD}\eta_{\text{diff}}E_0^2 J_1(\beta)\cos(\omega_{RF}t+\psi) \end{aligned} \tag{A.4}$$

The RF output power produced by $I_{RF}(t)$ over an internal charge R amplified with gain G reads:

$$\begin{aligned} P_{\text{out}} &= G\left\langle RI_{RF}(t)^2\right\rangle \\ &= \frac{GR}{2}\left(\eta_{11}\eta_{12}\eta_{21}\eta_{22}\ \eta_{PD}\eta_{\text{diff}}\right)^2 E_0^4 J_1(\beta)^2 \end{aligned} \tag{A.5}$$

With Z_{MZM} the input impedance of the phase modulator the RF input power reads:

$$P_{\text{in}} = \frac{\left\langle\left(V_{RF}\sin(\omega_{RF}t)\right)^2\right\rangle}{Z_{\text{MZM}}} \tag{A.6}$$

$$= \frac{V_{RF}^2}{2Z_{\text{MZM}}} = \frac{1}{2Z_{\text{MZM}}}\left(\frac{V_{\pi,RF}}{\pi}\right)^2\beta^2 \tag{A.7}$$

Assuming that $\beta \ll \pi$ and with (A.7) we have:

$$J_1(\beta)^2 \simeq \left(\frac{\beta}{2}\right)^2 = \frac{P_{\text{in}}Z_{\text{MZM}}}{2}\left(\frac{\pi}{V_{\pi,RF}}\right)^2 \tag{A.8}$$

We replace the expression of $J_1(\beta)^2$ from (A.8) in (A.5) and noting that $E_0^2 \propto P_0$ we finally have:

$$\boxed{\frac{P_{\text{out}}}{P_{\text{in}}} \propto P_0^2\left(\frac{\pi}{V_{\pi,RF}}\right)^2 Z_{\text{MZM}}\eta_{\text{diff}}\mathcal{R}_L^2 GR} \tag{A.9}$$

APPENDIX B
OPTICAL FIELD TRANSMISSION BY THE CRYSTAL & COMPLEX FIELD TRANSMISSION OF THE SHB FILTER

For clarity, in appendix A we omitted the frequency dependence of the diffraction efficiency of the crystal η_{diff} and did not consider the shape of the filter. The objective of this section is to express the frequency dependence of the RF transfer function $H(\nu)$ of the filter. We first derive the optical transfer function $H_{opt}(\nu)$ of the optical filter, corresponding to the diffraction by the crystal. Here ν is the optical frequency. The diffraction efficiency is then given by:

$$\eta_{\text{diff}}(\nu) = |H_{opt}(\nu)|^2 \tag{B.1}$$

The derivation relies on light-matter interaction theory. It unfolds as follows: on the one hand the two programming beams - indexed with 1 for the first one and 2 for the delayed one - are repeatedly sent on the crystal, optically pumping the ions until the susceptibility of the crystal reaches a steady state. We then send the signal beam - indexed with 3 - which polarizes the crystal due to the crystal susceptibility. This produces the diffracted beam - indexed with 4 - according to the wave equation (the beams indexing corresponds to Fig.1). We derive the response of the crystal to an excitation by a monochromatic signal beam, without

any assumption on the temporal shape of the programming beams. We describe the electromagnetic fields as plane waves.

As derived in section 4.2.1 from [22] with the hypothesis of :

1) short excitations compared to the excited state lifetime
2) short programming repetition rate compared to the metastable state lifetime
3) optically thin crystal

the complex susceptibility of the crystal at steady state after several repetitions of the two programming beams reads:

$$\chi(\vec{r},t) = \frac{2\pi\mu^2}{\hbar\varepsilon_0} e^{-\Gamma_h t} Y(t) \times \int_{-\infty}^{+\infty} \sin(2\pi\nu t) \left(1 - \frac{1}{\gamma T_P}\left(\left|\tilde{\Omega}_1 + \tilde{\Omega}_2\right|^2 \otimes \mathcal{L}_h\right)(\vec{r}, \nu - \nu_P)\right) \mathrm{d}\nu \tag{B.2}$$

where $\otimes$ is the convolution product of variable ν, μ is the dipole moment of the optical transition, $\mathcal{L}_h$ is the lorentzian homogeneous lineshape of the optical transition of width Γ_h, $Y(t)$ is the Heaviside function, γ is the relaxation rate of the metastable state into the fundamental state, T_P is the programming repetition period and $\nu_P = \nu_1 = \nu_2$ is the center frequency of the programming beams 1 and 2.

$\Omega_{1,2}$ stands for the complex Rabi frequency of beam $1, 2$: if the electric field reads $E(\vec{r},t) = A(t)e^{i\vec{k}\cdot\vec{r} - 2i\pi\nu_P t}$ then $\Omega = \frac{\mu}{\hbar} A(t) e^{i\vec{k}\cdot\vec{r}}$. The optically thin crystal hypothesis implies that A is constant over the crystal and so does not depend on $\vec{r}$.

$\tilde{f}$ or $F[f]$ stands for the Fourier tranform of function f defined as:

$$\tilde{f}(\nu) = F[f](\nu) = \int_{-\infty}^{+\infty} f(t) e^{2i\pi\nu t} \mathrm{d}t \tag{B.3}$$

By developing $\left|\tilde{\Omega}_1 + \tilde{\Omega}_2\right|^2$ in (B.2) we see three contributions in χ, one depending on $1 - \frac{1}{\gamma T_P}\left(\left|\tilde{\Omega}_1\right|^2 + \left|\tilde{\Omega}_2\right|^2\right) \otimes \mathcal{L}_h$, one on $\frac{1}{\gamma T_P}\left(\tilde{\Omega}_1^* \tilde{\Omega}_2\right) \otimes \mathcal{L}_h$ and one on $\frac{1}{\gamma T_P}\left(\tilde{\Omega}_1 \tilde{\Omega}_2^*\right) \otimes \mathcal{L}_h$. If we perform the derivation for all three contributions we see that they respectively describe the orders of diffraction 0, +1 and -1 of the signal beam by the grating in the crystal. In practice we only observe order +1 so we only consider the contribution depending on $\frac{1}{\gamma T_P}\left(\tilde{\Omega}_1^* \tilde{\Omega}_2\right) \otimes \mathcal{L}_h$:

$$\chi_{+1}(\vec{r},t) = -\frac{2\pi\mu^2}{\hbar\varepsilon_0\gamma T_P} e^{-\Gamma_h t} Y(t) \times \int_{-\infty}^{+\infty} \left[\left(\tilde{\Omega}_1^* \tilde{\Omega}_2\right) \otimes \mathcal{L}_h\right](\vec{r}, \nu - \nu_P) \sin(2\pi\nu t) \mathrm{d}\nu \tag{B.4}$$

By developing $\sin(2\pi\nu t) = \frac{e^{2i\pi\nu t} - e^{-2i\pi\nu t}}{2i}$ and noting that $F^{-1}[\mathcal{L}_h](t) = e^{-\Gamma_h |t|}$ we rewrite (B.4):

$$\chi_{+1}(\vec{r},t) = -\frac{2\pi\mu^2}{\hbar\varepsilon_0\gamma T_P} e^{-\Gamma_h t} Y(t) e^{-\Gamma_h |t|} \frac{1}{2i} \times \left(F^{-1}\left[\tilde{\Omega}_1^* \tilde{\Omega}_2\right](\vec{r}, -t) e^{2i\pi\nu_P t} - F^{-1}\left[\tilde{\Omega}_1^* \tilde{\Omega}_2\right](\vec{r}, t) e^{-2i\pi\nu_P t}\right) \tag{B.5}$$

According to the linear response theory, the polarization produced by the susceptibility and the exciting signal beam E_3 is $\tilde{P}(\vec{r},\nu) = \varepsilon_0 \tilde{E_3}(\vec{r},\nu)\tilde{\chi}_{+1}(\vec{r},\nu)$:

$$\tilde{P}(\vec{r},\nu) = \tilde{E_3}(\nu) \frac{i\pi\mu^2}{\hbar\gamma T_P} F\Big[e^{-2\Gamma_h t} Y(t) \times \left(F^{-1}\left[\tilde{\Omega}_1^* \tilde{\Omega}_2\right](\vec{r}, -t) e^{2i\pi\nu_P t} - F^{-1}\left[\tilde{\Omega}_1^* \tilde{\Omega}_2\right](\vec{r}, t) e^{-2i\pi\nu_P t}\right)\Big](\nu) \tag{B.6}$$

$F\left[e^{-2\Gamma_h t} Y(t) F^{-1}\left[\tilde{\Omega}_1^* \tilde{\Omega}_2\right](\vec{r}, -t)\right]$ is a function centered around $\nu = 0$ as a product of functions centered around $\nu = 0$, so $F\left[e^{-2\Gamma_h t} Y(t) F^{-1}\left[\tilde{\Omega}_1^* \tilde{\Omega}_2\right](\vec{r}, -t) e^{2i\pi\nu_P t}\right]$ is centered around $\nu = -\nu_P < 0$. Since $\tilde{E_3}$ is centered around $\nu = +\nu_3 > 0$, their domains are disjoints so the contribution of this term is null. We finally obtain, noting that $F\left[f(t) e^{-2i\pi\nu_P t}\right](\nu) = F[f](\nu - \nu_P)$:

$$\tilde{P}(\vec{r},\nu) = \tilde{E_3}(\nu) \frac{\pi\mu^2}{i\hbar\gamma T_P} \times F\left[e^{-2\Gamma_h t} Y(t) F^{-1}\left[\tilde{\Omega}_1^* \tilde{\Omega}_2\right](\vec{r}, t)\right](\nu - \nu_P) \tag{B.7}$$

In our case beam 2 is identical to beam 1 but delayed and with a different angle of incidence on the crystal. So we write $\Omega_1(\vec{r},t) = \frac{\mu}{\hbar} A_1(t) e^{i\vec{k_1}\cdot\vec{r}}$ and $\Omega_2(\vec{r},t) = \frac{\mu}{\hbar} A_1(t-\tau) e^{i\vec{k_2}\cdot\vec{r} + 2i\pi\nu_P\tau}$. Since we look for the filter response to a monochromatic excitation we also take $\tilde{E_3}(\vec{r},\nu) = A_3 e^{i\vec{k_3}\cdot\vec{r}} \delta_{\nu_3}(\nu)$. Noting that $F[A_1(t-\tau)](\nu) = \tilde{A_1}(\nu) e^{2i\pi\nu\tau}$ we can rewrite (B.7):

$$\boxed{\tilde{P}(\vec{r},\nu) = A_3 \delta_{\nu_3}(\nu) \frac{\pi\mu^4}{i\hbar^3\gamma T_P} e^{2i\pi\nu_P\tau} \times F\left[e^{-2\Gamma_h t} Y(t) F^{-1}\left[|\tilde{A_1}|^2 e^{2i\pi\nu\tau}\right](t)\right](\nu - \nu_P) e^{i(\vec{k_3} + \vec{k_2} - \vec{k_1})\cdot\vec{r}}} \tag{B.8}$$

Now that we have derived the polarization, the wave equation provides us the diffracted beam. Assuming that all beams share the same polarization and that the diffracted beam E_4 is a plane wave propagating along $z = \vec{r}\cdot\vec{u_4}$ the frequency form of the wave equation reads :

$$\frac{\partial^2 \tilde{E_4}}{\partial z^2}(z,\nu) + \left(\frac{2\pi\nu}{c}\right)^2 \tilde{E_4}(z,\nu) = -\left(\frac{2\pi\nu}{c}\right)^2 \frac{1}{\varepsilon_0} \tilde{P}(\vec{r}\cdot\vec{u_4},\nu) \tag{B.9}$$

This differential equation is solved analitically by rewriting it under the shape of a first order vectorial differential equation and using the variation of constants method. With L the length of the crystal we obtain:

$$\tilde{E_4}(L,\nu) = -\frac{2\pi\nu}{c}\int_0^L \sin\left(\frac{2\pi\nu}{c}(L-z)\right)\frac{1}{\varepsilon_0}\tilde{P}(z\vec{u_4},\nu)\mathrm{d}z \tag{B.10}$$

Injecting (B.8) in (B.10) we find:

$$\begin{aligned}\tilde{E_4}(L,\nu) = A_3\delta_{\nu_3}(\nu)\frac{2i\pi^2\mu^4\nu_3}{c\hbar^3\varepsilon_0\gamma T_P}e^{2i\pi\nu_P\tau}\ \times \\ F\left[e^{-2\Gamma_h t}Y(t)F^{-1}\left[|\tilde{A_1}|^2e^{2i\pi\nu\tau}\right](t)\right](\nu_3-\nu_P)\ \times \\ \int_0^L \sin\left(\frac{2\pi\nu_3}{c}(L-z)\right)e^{i(\vec{k_3}+\vec{k_2}-\vec{k_1})\cdot z\vec{u_4}}\mathrm{d}z\end{aligned} \tag{B.11}$$

Now let us simplify the spatial integral of (B.11). The phase matching condition in a three beams echo experiment like ours implies that $\vec{k_4} = \vec{k_3} + \vec{k_2} - \vec{k_1}$ and that $\vec{k_4} = \frac{2\pi\nu_3}{c}\vec{u_4}$, which gives:

$$\begin{aligned}&\int_0^L \sin\left(\frac{2\pi\nu_3}{c}(L-z)\right)e^{i(\vec{k_3}+\vec{k_2}-\vec{k_1})\cdot z\vec{u_4}}\mathrm{d}z \\ &= \frac{1}{2i}\int_0^L\left[e^{\frac{2i\pi\nu_3}{c}(L-z)} - e^{-\frac{2i\pi\nu_3}{c}(L-z)}\right]e^{\frac{2i\pi\nu_3}{c}z}\mathrm{d}z \\ &= \frac{1}{2i}\int_0^L e^{\frac{2i\pi\nu_3}{c}L} - e^{\frac{2i\pi\nu_3}{c}(L-2z)}\mathrm{d}z\end{aligned} \tag{B.12}$$

We neglect the rapidly oscillating $e^{\frac{2i\pi\nu_3}{c}(L-2z)}$ part and obtain:

$$\int_0^L \sin\left(\frac{2\pi\nu_3}{c}(L-z)\right)e^{i(\vec{k_3}+\vec{k_2}-\vec{k_1})\cdot z\vec{u_4}}\mathrm{d}z = \frac{L}{2i}e^{\frac{2i\pi\nu_3}{c}L} \tag{B.13}$$

Injecting (B.13) in (B.10) we can write the optical transfer function defined as $H_{opt}(\nu_3) = \frac{\tilde{A_4}(L,\nu_3)}{A_3} = \frac{\tilde{E_4}(L,\nu_3)e^{-\frac{2i\pi\nu_3}{c}L}}{A_3}$:

$$\begin{aligned}H_{opt}(\nu) =&\frac{\pi^2\mu^4\nu L}{c\hbar^3\varepsilon_0\gamma T_P}e^{2i\pi\nu_P\tau}\times \\ &F\left[e^{-2\Gamma_h t}Y(t)F^{-1}\left[|\tilde{A_1}|^2e^{2i\pi\nu\tau}\right](t)\right](\nu-\nu_P)\end{aligned} \tag{B.14}$$

Note that, in particular due to the hypothesis of optically thin crystal, the amplitude of $t(\nu)$ is largely misestimated by this derivation. However, as demonstrated in section III, the spectral shape is very accurate. One should retain the following expression:

$$H_{opt}(\nu) \propto F\left[e^{-2\Gamma_h t}Y(t)F^{-1}\left[|\tilde{A_1}|^2e^{2i\pi\nu\tau}\right](t-\tau)\right](\nu-\nu_P) \tag{B.15}$$

With $F[f\times g] = F[f]\otimes F[g]$ we can reformulate B.15:

$$H_{opt}(\nu) \propto \left[\left(|\tilde{A_1}|^2e^{2i\pi\nu\tau}\right)\otimes\mathcal{L}_h\otimes\mathcal{L}_h\otimes\tilde{Y}\right](\nu-\nu_P) \tag{B.16}$$

We obtain the RF transfer function by downconverting H_{opt} with the local oscillator frequency ν_0. Here $\nu_0 = \nu_3$. Considering A.9, B.1 and B.16 we finally find the RF transfer function $H(\nu)$ of the SHB filter, with $|H(\nu)|^2 = T(\nu) = P_{\mathrm{out}}(\nu)/P_{\mathrm{in}}$:

$$H(\nu) \propto \left[\left(|\tilde{A_1}|^2e^{2i\pi\nu\tau}\right)\otimes\mathcal{L}_h\otimes\mathcal{L}_h\otimes\tilde{Y}\right](\nu-(\nu_P-\nu_0)) \tag{B.17}$$

REFERENCES

[1] K. D. Merkel, W. R. Babbitt, Z. W. Barber, and S. H. Bekker, "Extreme wideband photonic cueing receiver for electronic support: Cswap and fidelity comparisons to an all-digital alternative," in *GOMACTech 2013 conference*, 2013, pp. 11–14.

[2] S. Gupta, S. Abielmona, and C. Caloz, "Microwave analog real-time spectrum analyzer (rtsa) based on the spectral–spatial decomposition property of leaky-wave structures," *IEEE Transactions on Microwave Theory and Techniques*, vol. 57, no. 12, pp. 2989–2999, 2009.

[3] D. Onori, F. Scotti, F. Laghezza, M. Bartocci, A. Zaccaron, A. Tafuto, A. Albertoni, A. Bogoni, and P. Ghelfi, "A photonically enabled compact 0.5–28.5 GHz RF scanning receiver," *Journal of Lightwave Technology*, vol. 36, no. 10, pp. 1831–1839, 2018.

[4] J. R. G. Oya, F. Muñoz, A. Torralba, A. Jurado, A. Garrido, and J. Banos, "Data acquisition system based on subsampling for testing wideband multistandard receivers," *IEEE Transactions on Instrumentation and Measurement*, vol. 60, no. 9, pp. 3234–3237, 2011.

[5] M. S. Alshaykh, D. E. Leaird, J. D. McKinney, and A. M. Weiner, "Rapid wideband rf subsampling and disambiguation using dual combs," in *CLEO: Science and Innovations*. Optical Society of America, 2019, pp. SF2N–8.

[6] J. Kim, M. J. Park, M. H. Perrott, and F. X. Kärtner, "Photonic subsampling analog-to-digital conversion of microwave signals at 40 GHz with higher than 7 ENOB resolution," *Optics Express*, vol. 16, no. 21, pp. 16 509–16 515, 2008.

[7] P. Ghelfi, F. Scotti, D. Onori, and A. Bogoni, "Photonics for ultrawideband rf spectral analysis in electronic warfare applications," *IEEE Journal of Selected Topics in Quantum Electronics*, vol. 25, no. 4, pp. 1–9, 2019.

[8] Z. Tang, D. Zhu, and S. Pan, "Coherent optical rf channelizer with large instantaneous bandwidth and large in-band interference suppression," *Journal of Lightwave Technology*, vol. 36, no. 19, pp. 4219–4226, 2018.

[9] P. Berger, Y. Attal, M. Schwarz, S. Molin, A. Louchet-Chauvet, T. Chanelière, J.-L. Le Gouët, D. Dolfi, and L. Morvan, "Rf spectrum analyzer for pulsed signals: ultra-wide instantaneous bandwidth, high sensitivity, and high time-resolution," *Journal of Lightwave Technology*, vol. 34, no. 20, pp. 4658–4663, 2016.

[10] K. D. Merkel, S. H. Bekker, A. S. Traxinger, C. R. Stiffler, A. J. Woidtke, M. D. Chase, W. R. Babbitt, Z. W. Barber, and C. H. Harrington, "20 GHz instantaneous bandwidth rf spectrum analyzer measurements with high sensitivity and spur free dynamic range," in *Proceedings of the GOMAC2014 Conference, Charleston, SC*, 2014.

[11] J. Hogan, W. R. Babbitt, C. Benko, S. Bekker, C. Stiffler, K. Winn, R. Price, and K. Merkel, "Assured capture of transient rf events across extremely wide bandwidths," in *2019 IEEE Research and Applications of Photonics in Defense Conference (RAPID)*. IEEE, 2019, pp. 1–4.

[12] P. Li, X. Zou, W. Pan, L. Yan, and S. Pan, "Tunable photonic radiofrequency filter with an ultra-high out-of-band rejection," *arXiv preprint arXiv:1611.05553*, 2016.

[13] S. Cai, G. Choo, B. Wang, K. Entesari, and S. Palermo, "Comprehensive adaptive tuning of silicon rf photonic filters," in *2016 Texas Symposium on Wireless and Microwave Circuits and Systems (WMCS)*. IEEE, 2016, pp. 1–4.

[14] R. S. Guzzon, E. J. Norberg, J. S. Parker, L. A. Johansson, and L. A. Coldren, "Monolithically integrated programmable photonic microwave filter with tunable inter-ring coupling," in *2010 IEEE International Topical Meeting on Microwave Photonics*. IEEE, 2010, pp. 23–26.

[15] A. Choudhary, Y. Liu, D. Marpaung, and B. J. Eggleton, "On-chip brillouin filtering of rf and optical signals," *IEEE journal of selected topics in quantum electronics*, vol. 24, no. 6, pp. 1–11, 2018.

[16] M. S. Rasras, D. M. Gill, S. S. Patel, K.-Y. Tu, Y.-K. Chen, A. E. White, A. T. Pomerene, D. N. Carothers, M. J. Grove, D. K. Sparacin *et al.*, "Demonstration of a fourth-order pole-zero optical filter integrated using cmos processes," *Journal of Lightwave Technology*, vol. 25, no. 1, pp. 87–92, 2007.

[17] Z. Serahati, E. Temprana, E. Myslivets, V. Ataie, N. Alic, and S. Radic, "Demonstration of a sub-ghz flat-top comb-based rf-photonic filter enabled by fourth-order dispersion compensation," *Journal of Lightwave Technology*, vol. 38, no. 6, pp. 1194–1201, 2019.
[18] R. Reibel, Z. Barber, M. Tian, and W. Babbitt, "Temporally overlapped linear frequency-chirped pulse programming for true-time-delay applications," *Optics letters*, vol. 27, no. 7, pp. 494–496, 2002.
[19] H. Linget, T. Chanelière, J.-L. Le Gouët, P. Berger, L. Morvan, and A. Louchet-Chauvet, "Interlaced spin grating for optical wave filtering," *Physical Review A*, vol. 91, no. 2, p. 023804, 2015.
[20] I. Lorgeré, L. Menager, V. Lavielle, J.-L. Le Gouët, D. Dolfi, S. Tonda, and J.-P. Huignard, "Demonstration of a radio-frequency spectrum analyser based on spectral hole burning," *journal of modern optics*, vol. 49, no. 14-15, pp. 2459–2475, 2002.
[21] C. W. Thiel, R. L. Cone, and T. Böttger, "Laser linewidth narrowing using transient spectral hole burning," *Journal of luminescence*, vol. 152, pp. 84–87, 2014.
[22] V. Lavielle, "Processus atomiques coherents appliques a l'analyse spectrale tres large bande de signaux radio frequence," Ph.D. dissertation, Universite Paris Sud-Paris XI, 2004.

Lothaire Ulrich received the engineering degree from Ecole Centrale Paris, Gif-sur-Yvette, France, in 2019, and the Master of Science degree in Nanophysics from Université Paris-Saclay, in 2019. In 2018, he started working toward the Ph.D. degree in physics both in Thales R&T, Palaiseau, France and Paris Sciences & Lettres, CNRS, Institut Langevin, Paris, France.

Sacha Welinski received a M.S. degree in physics from the Ecole Supérieure de Physique et de Chimie Industrielles (ESPCI ParisTech) and from Sorbone Université (Paris). He obtained his PhD in 2018 from Paris Science & Lettres university (CNRS) on paramagnetic-rare-earth-doped single crystals for quantum information processing. He then occupied a postdoctoral position at Princeton University (USA) where he investigated the interest of color centers in diamond for quantum applications. He joined TRT in 2020. His research is now focused on microwave photonics and quantum technologies.

Anne Louchet-Chauvet received the M.S. degree from the Ecole Normale Supérieure, Lyon, France, and the Ph.D. degree in physics from the Université Paris-Sud, France, in 2008. She is now a permanent CNRS researcher at Institut Langevin, Paris. Her research interests include classical information processing using spectral holeburning and photon echoes in rare-earth ion-doped crystals, including spectral analysis of optically-carried RF signals, time reversal, and filtering.

Julien de Rosny received the M.S. degree from the University Pierre et Marie Curie, Paris, France, in 1996 and the Ph.D. degree from the same university in 2000, both in wave physics. During the 2000–2001 academic year, he was a postdoctoral fellow in the Marine Physical Laboratory at Scripps Research Institute, La Jolla, CA, USA. In 2001, he became a junior scientist of the Centre National de la Recherche Scientifique (CNRS) at the Laboratoire Ondes et Acoustique, Paris, France. Since 2014, he has been a CNRS senior scientist at the Institut Langevin, Paris, France. His fields of interest include wave propagation and time reversal of waves in complex media, and passive and active imaging applied to acoustic, elastic, and electromagnetic waves.

Daniel Dolfi received the Graduate degree from Ecole Supŕieure d'Optique, Palaiseau, France, in 1986, the Ph.D. degree from University Paris XI, Orsay, France, in 1993, and "Habilitation à Diriger des Recherches" in 2008. He is currently the Director of the Physics Department in Thales R&T. His main research interests include optoelectronic generation and processing of microwave and THz signals, non-linear optics and sensing in fibers, opto-electronic devices and sub-systems, lidars and active imaging systems. He has about 80 publications in refereed journals, 130 communications in international conferences, and 60 patents. He is EOS Fellow and OSA Fellow.

Perrine Berger received the Master's degree in physics from the Ecole Supérieure de Physique et Chimie Industrielles (ESPCI ParisTech), France, in 2008 and the Ph.D. degree in physics from the University of Paris-Sud, Paris, in 2012, with a thesis on slow and fast light for applications in microwave photonics and RADAR. Since 2012, she has been Research Scientist in Thales Research and Technology, Palaiseau, France. Her research interests include spectral hole burning in rare earth doped crystals, optically assisted analogue to digital converters and microwave photonics.

Loïc Morvan received the Master's degree in fundamental physics in 1998 and the Ph.D degree in optoelectronics from the University Paris XI, Orsay, France, in 2006. He joined Thales R&T, France, in 2001 as a research staff member. He is currently Head of "Laboratoire Onde et Traitement du Signal", Thales R&T, France. His research interests include the optoelectronic generation and processing of microwave and THz signals and high resolution lidar systems.